ADVANCED ENERGY MATERIALS
www.advenergymat.de

Evaporation-Free Nonfullerene Flexible Organic Solar Cell Modules Manufactured by An All-Solution Process

*Yong Woon Han, Sung Jae Jeon, Hyoung Seok Lee, Hongkwan Park, Kwang Su Kim, Ho-Won Lee, and Doo Kyung Moon**

To ensure laboratory-to-industry transfer of next-generation energy harvesting organic solar cells (OSCs), it is necessary to develop flexible OSC modules that can be produced on a continuous roll-to-roll basis and to apply an all-solution process. In this study, nonfullerene acceptors (NFAs)-based donor polymer, SMD2, is newly designed and synthesized to continuously fabricate high-performance flexible OSC modules. Also, multifunctional hole transport layers (HTLs), WO_3/HTL solar bilayer HTLs, are developed and applied via an all-solution process called "ProcessOne" into inverted structure. SMD2, the donor terpolymer, has a deep highest occupied molecular orbital (HOMO) level and can achieve a power conversion efficiency (PCE) of 11.3% with NFAs without any pre-/post-treatment because of its optimal balance between crystallinity and miscibility. Furthermore, the integration of multifunctional HTLs enables the recovery of the drop in open circuit voltage (V_{OC}) caused by a mismatch in energy levels between the deep HOMO level of the NFAs-based bulk-heterojunction layer and the solution-processed HTLs. Also, the photostability under ultraviolet-exposure necessary for "ProcessOne" is greatly improved because of the integration of multifunctional HTLs. Consequently, because of the synergistic effects of these approaches, the flexible OSC modules fabricated in an industrial production line have a PCE of 5.25% (P_{max} = 419.6 mW) on an active area of 80 cm^2.

1. Introduction

Organic solar cells (OSCs) are photoenergy conversion devices using an energy harvesting technique and have several advantages such as processability in solutions, the possibility of fabricated for application over a large area, and applicability in flexible electronics.[1–6] It is possible to design high-performance devices by designing photoactive materials that constitute a bulk heterojunction (BHJ),[7–9] device engineering,[10–13] and a combination of these.[14,15] Therefore, this has attention as an area in which commercialization can occur through the application of flexible, wearable, and portable devices, and building-integrated photovoltaics.[4,16–20] Recently, different methods such as spin coating,[21–23] slot-die coating,[24–26] and blade coating,[27,28] are being attempted to develop large-area modules with laboratory-to-industrial applications. Among them, slot-die coating can easily control each layer and the related processing factors, such as discharge rate and speed, thus enabling control of thickness and conformation. Therefore, it is the most appropriate coating method to use to produce devices and modules with large areas.[16,29]

Krebs and co-workers fabricated flexible OSC modules using a roll-to-roll (R2R) manufacturing process called "ProcessOne." Their flexible OSC modules with power conversion efficiencies (PCEs) of 2–3% demonstrated an energy payback time (EPBT) of 2.02–1.35 years.[30,31] Using ProcessOne, the BHJ layer and buffer layer were formed using slot-die coating and the Ag back electrode was formed via screen printing; this resulted in the design of OSC modules with inverted structures, which enabled cost-effective production.[32,33] Several particular challenges need to be considered in the manufacturing of this type of OSC modules using an R2R process; these included thermally treating the film[34,35] and ensuring the thermal stability of the substrate[36] the uniformity of the film morphology,[22–24] and the evaporation process of the buffer layer and the electrode.[3,25,26,37]

The large-area flexible OSC modules have been reported their efficiencies with various materials and coating methods. In flexible unit-cells with small-area, Peng and co-workers recently reported high PCE of 14.06% introducing ternary heterojunction strategy in active area of 0.04 cm^2.[38] The flexible OSC module based thermally evaporated top electrode reported relatively higher performances. Zhou and co-workers reported tandem structure with PCE of 6.5% in active area of 10.5 cm^2, also, Ma and co-workers reported ternary structure with PCE of

Dr. Y. W. Han, Dr. S. J. Jeon, H. S. Lee, Prof. D. K. Moon
Nano and Information Materials Lab. (NIMs Lab.)
Department of Chemical Engineering
Konkuk University
120 Neungdong-ro, Gwangjin-gu, Seoul 05029, Republic of Korea
E-mail: dkmoon@konkuk.ac.kr
Dr. H. Park, K. S. Kim
Energy & Environmental Lab.
KOLON Advanced Research Cluster
110 Magokdong-ro, Gangseo-gu, Seoul 07793, Republic of Korea
Prof. H-W. Lee
Department of Chemical and Biological Engineering
Jeju National University
102 Jejudaehak-ro, Jeju-si, Jeju-do 63243, Republic of Korea
The ORCID identification number(s) for the author(s) of this article can be found under https://doi.org/10.1002/aenm.201902065.

DOI: 10.1002/aenm.201902065

5.18% in active area of 20 cm^2.[26,39] However, the flexible OSC modules based solution-processed top electrode have reported various challenging attempts in large-area system. Krebs et al. reported flexible OSC modules fabricated via R2R process with PCE of 2.1% in active area of 120 cm^2.[40] Also, Machui and co-workers reported PCE of 5.0% in active area of 59.52 cm^2 focused on nonfullerene acceptors (NFAs) system and all-solution process for industrial scalable strategy.[29] Because of most researches of flexible OSC modules have been focused on fullerene acceptors (FAs) system and evaporated electrode, an in-depth study of focused on NFAs-based and all-solution process are necessary. Therefore, studies on 1) the design of high-performance photoactive materials without any pre-/post-treatment, 2) solution-processed device engineering, and 3) evaporation-free processing of electrodes can lead to the manufacture of high-performance flexible OSC modules using an all-solution process.

First, in terms of photoactive materials, conversion from the previously used FAs to NFAs allowed the rapid development of OSCs.[41–43] NFAs have relatively easier energy level tunability, which also have a high absorption coefficient and crystallinity compared with FAs. Therefore, NFAs are more advantageous for the development of high-performance OSCs.[41] Recently, NFAs-based OSCs showed high PCEs of 16% and 17%, respectively, for single and tandem cells.[6,42,43] However, most NFAs-based photoactive layer combinations require pre-/post-treatment processes to maximize their PCEs, which sometimes raises concerns regarding performance gaps between laboratory-to-industry.[44–48] Therefore, studies on NFAs-based donor and acceptor combinations for BHJ layers using pre-/post-treatment-free processes to achieve high performances are necessary for the application of flexible, large-area OSC modules.

Second, the selection of appropriate buffer layers, possible application of an R2R coating, and ease of processing are considered for manufacturing OSC modules using NFAs-based BHJ layers via solution processing. Therefore, it is necessary to develop a device structure and to consider efficient process to maximize performance of OSC modules.[3,4,29,49] The donors with deep highest occupied molecular orbital (HOMO) levels, in particular, are incorporated to achieve a high open circuit voltage (V_{OC}) in NFAs-based inverted structure OSCs. In these cases, the V_{OC} drop occurs due to interfacial interaction, wettability and energy level mismatch with photoactive layer and hole transport layers (HTLs) (particularly HTL Solar, a kind of modified-poly(2,3-dihydrothieno-1,4-dioxin):poly(styrene sulfonate), PEDOT:PSS).[50–53] When the BHJ layer is incorporated into an inverted structure OSCs through a solution process, the introduction of an appropriate buffer layer between the BHJ layer and the electrode is necessary to improve the interfacial electronic properties.[13,54] However, only a few studies have investigated solution-processed devices that contain an NFAs-based BHJ layer, and the incorporation of modified-buffer layer and dual buffer layer that allow energy level matching is also necessary.[54–56]

Furthermore, because a vacuum process is required for efficient modulation of OSCs, productivity decreases. Therefore, third, the formation of a buffer layer and electrode via slot-die coating and screen printing is necessary to manufacture OSC modules using an all-solution process.[25,26,32,33] During this process, the conductive silver (Ag) paste commonly used is usually treated by thermal and ultraviolet (UV) curing to fabricate electrodes.[32,33] Among them, UV-cured Ag electrodes have excellent electronic properties; however, the BHJ layer below the electrode may undergo photodegradation during UV-curing. Since the photostability of the NFAs-based BHJ layer is lower than that of the FAs system,[57,58] it is necessary to develop buffer layer technology for protecting the BHJ layers.

Therefore, in this study, a new random building block donor terpolymer, SMD2, was designed and synthesized to manufacture efficient and high-performance NFAs-based flexible OSC modules via "ProcessOne." The SMD2 was induced to have optimal balance between crystallinity and miscibility by modifying the restricted structure of a well-known donor polymer, poly[(2,6-(4,8-bis(5-(2-ethylhexyl)thiophen-2-yl)-benzo[1,2-b:4,5-b′]dithiophene))-alt-(5,5-(1′,3′-di-2-thienyl-5′,7′-bis(2-ethylhexyl) benzo[1′,2′-c:4′,5′-c′]dithiophene-4,8-dione)] (PBDB-T), which was controlled to increase the regio-random segments in the polymer backbones. SMD2 achieved a high PCE of 11.3%, compared to PBDB-T, without any pre-/post-treatment when combined with NFAs-based on its high molar absorption coefficient, deep HOMO level, and balanced crystalline structure.

Also, multifunctional HTLs with a bilayer WO_3/HTL Solar structure were introduced in a SMD2-based OSCs system via the solution process to improve the photostability and match the energy level of HTL Solar.[59–62] Through this approach, the internal potential and interfacial contact was improved and the unit cells achieved a PCE of 10.3% with excellent photostability under UV-exposure.

Finally, SMD2-based BHJ layer and multifunctional bilayer HTLs were introduced via the slot-die coating to produce inverted structure flexible OSC modules. The flexible OSC modules consisted of 10 cells connected in a series and achieved a maximum PCE of 5.25% (V_{OC} = 8.80 V). Since a high performance could be achieved by the evaporation-free process, it is appropriate for application in continuous processes. Furthermore, it is an innovative strategy for achieving high-performance NFAs-based flexible OSC modules.

2. Results and Discussion

2.1. Design and Characterization of SMD2

Generally, random donor copolymers have a higher solubility but a lower crystallinity than alternating copolymers, which sometimes causes problems in terms of compatibility with the acceptors.[63,64] In addition, the random copolymer strategy has mainly been excluded because of large batch-to-batch variation can occur during the synthesis process.[64] However, the SMD2 of random building blocks was successfully designed and synthesized by structurally modifying the well-known donor polymer PBDB-T. As shown in Scheme S1 and Figures S1–S3 (Supporting Information), SMD2 was developed by restricting the D1:A1 contents at a ratio of 1:1 in the PBDB-T, converting it to D1:D2:A1 at a ratio of 0.5:0.5:1 with D2, which is structurally similar to D1. The D2 unit is composed of two 2-ethylhexylthio chains of 2D benzo[1,2-c:4,5-c′]dithiophene (2DBDT) cores instead of 2-ethylhexyl chains of D1 that could improve the

Table 1. Physical, optical and electrochemical properties for PBDB-T and SMD2.

Polymer	GPC			UV–visible absorption			Cyclic voltammetry		
	M_n[a)] [kDa]	M_w[a)] [kDa]	PDI[a)]	Chloroform solution	Molar absorption coefficient	Film	$E_g^{opt,b)}$ [eV]	E_{HOMO}[c)] [eV]	E_{LUMO}[c)] [eV]
				λ_{max} [nm]	ε [M^{-1} cm^{-1}] at λ_{max} [nm]	λ_{max} [nm]			
PBDB-T	26.942	70.683	2.624	359, 620	30516 (359), 73529 (620)	377, 627	1.80	−5.40	−3.60
SMD2	41.442	103.968	2.509	363, 615	33973 (363), 75276 (615)	379, 630	1.78	−5.44	−3.66

[a)]The parameters (M_n: number-average molecular weight; M_w: weight-average molecular weight; PDI: polydispersity index) determined by GPC in chloroform using polystyrene standards; [b)]Calculated from the intersection of the tangent on the low energetic edge of the absorption spectrum with the baseline; [c)]$E_{HOMO} = -[E_{ox}^{onset}$ (vs Ag/AgCl) $- E_{1/2}(Fc/Fc^+$ vs Ag/AgCl)] − 4.8 eV ($E_{1/2}(Fc/Fc^+$ vs Ag/AgCl) = 0.49 eV, experimental data), $E_{LUMO} = E_g^{opt} - E_{HOMO}$.

crystallinity, molar coefficient, and oxidation stability of SMD2. Furthermore, this change in the polymer backbones produced significant tilting (from 69.4° to 81.7°) on the unshared electron pair in sulfur, as determined by density functional theory (DFT) calculations (Figure S4, Supporting Information). Therefore, a high degree of polymerization might be expected because of the increase in regio-random segments and the improved solubility caused by the steric hindrance of the polymer backbones.[65]

As shown in Scheme S1 (Supporting Information), the D1-A1-D2-A1-type random building block donor terpolymer SMD2 was newly synthesized via the Stille coupling reaction with a high yield of 90%. SMD2 easily dissolved in common organic solvents such as chloroform, chlorobenzene, and *o*-dichlorobenzene without requiring any post-treatment such as annealing. The chemical structure of SMD2 was confirmed by ^{1}H nuclear magnetic resonance (NMR) spectroscopy and elemental analysis (EA) (Figures S1–S3, Supporting Information). The detailed physical, optical, and electrochemical properties of PBDB-T and SMD2 are summarized in **Table 1**. Gel permeation chromatography (GPC) results showed that SMD2 has a higher number-average molecular weight (M_n = 41.442 kDa), weight-average molecular weight (M_w = 103.968 kDa), and a narrow polydispersity index (PDI = 2.509) compared to PBDB-T (M_n = 26.942 kDa, M_w = 70.683 kDa, and PDI = 2.624). Thermogravimetric analysis (TGA) showed that PBDB-T and SMD2 lost 5% of their weight at 366 and 330 °C, respectively (Figure S5, Supporting Information). This difference was because of the incorporation of sulfur chains and the increase in regio-random segments in the molecular structure. However, the thermal stability of both polymers was sufficiently high and enough for application in OSCs.[66] Differential scanning calorimetry (DSC), which was used to analyze the crystalline natures of the polymers at temperatures ranging from room temperature to 290 °C, showed no characteristic peaks (Figure S6, Supporting Information).

The energy levels, dipole moments, and electrostatic potentials (ESP) were calculated using geometric optimization for different repeating units (n), 2 or 4 for SMD2 and PBDB-T using computational simulation (Figure S7, Supporting Information). The calculated top and side views showed that the two polymers had similar curvatures with high planarity. As shown in Figure S7a–c (Supporting Information), SMD2 had a slightly decreased HOMO level (0.084 eV) and an increased dipole moment (0.03 D) than PBDB-T at the optimized geometries at n = 2 for both polymers. In addition, SMD2 showed almost identical bandgap energy with PBDB-T by incorporating the D2 unit in the polymer backbone (detailed parameters are shown in Table S1 in the Supporting Information). We calculated the ESP at n = 4 at extended conjugation lengths to precisely determine the electrostatic difference in PBDB-T and SMD2. The result showed that among the conjugated polymer backbones, both polymers had dominant continuous positive charge potentials.[67] Furthermore, with the incorporation of the D2 unit, the sulfur chains showed a partial negative charge potential. These phenomena show that the D2 unit has stronger electron donating properties in the polymer backbone than the D1 unit, which decreases effectively the bandgap by its push-pull structure (Figure S7d, Supporting Information).[67,68]

The optical and electrochemical properties of PBDB-T and SMD2 were measured by UV–vis spectroscopy and cyclic voltammetry (CV) (Figure S8, Supporting Information). Both polymers showed two distinct absorption bands at λ = 300–450 and 500–700 nm based on the π–π^* transition and the intramolecular charge transfer from the donor to the acceptor units. Although SMD2 exhibited a smaller absorption edge onset in the solution states, the optical bandgap of SMD2 decreased by 0.02 eV in the film states. This means that the random building blocks of SMD2 had lower aggregation effects than PBDB-T in the solution state because of structural complexity and irregularity; therefore, π–π stacking increased and recovered in the film state and led to higher aggregation effects.[64,69] The results showed that SMD2 increased by ε (calculated from the Lambert–Beer equation) with 3457 and 1747 M^{-1} cm^{-1} at maximum absorption peaks (λ_{max}) for short and long wavelengths; these were slightly higher than those of PBDB-T. In terms of energy levels, SMD2 had a deep-lying HOMO level of 0.04 eV deeper than PBDB-T; especially, HOMO levels of PBDB-T and SMD2 were characterized as −5.40 and −5.44 eV, respectively (as shown in Table 1). These results were consistent with the trends in computational simulations (Figure S8c, Supporting Information).

2.2. Relationship Between Crystallinity and Miscibility of Photoactive Materials

Based on the molecular design strategy, SMD2 with increasing regio-random segments in the molecular structure was induced to have an optimal balance between crystallinity and miscibility with diverse NFAs compared with PBDB-T. To confirm the pristine molecular orientation and packing order properties of the donor polymers (PBDB-T and SMD2) and NFAs (ITIC and ITIC-Th), they were analyzed by grazing-incidence wide-angle X-ray scattering (GIWAXS), the results of which are shown

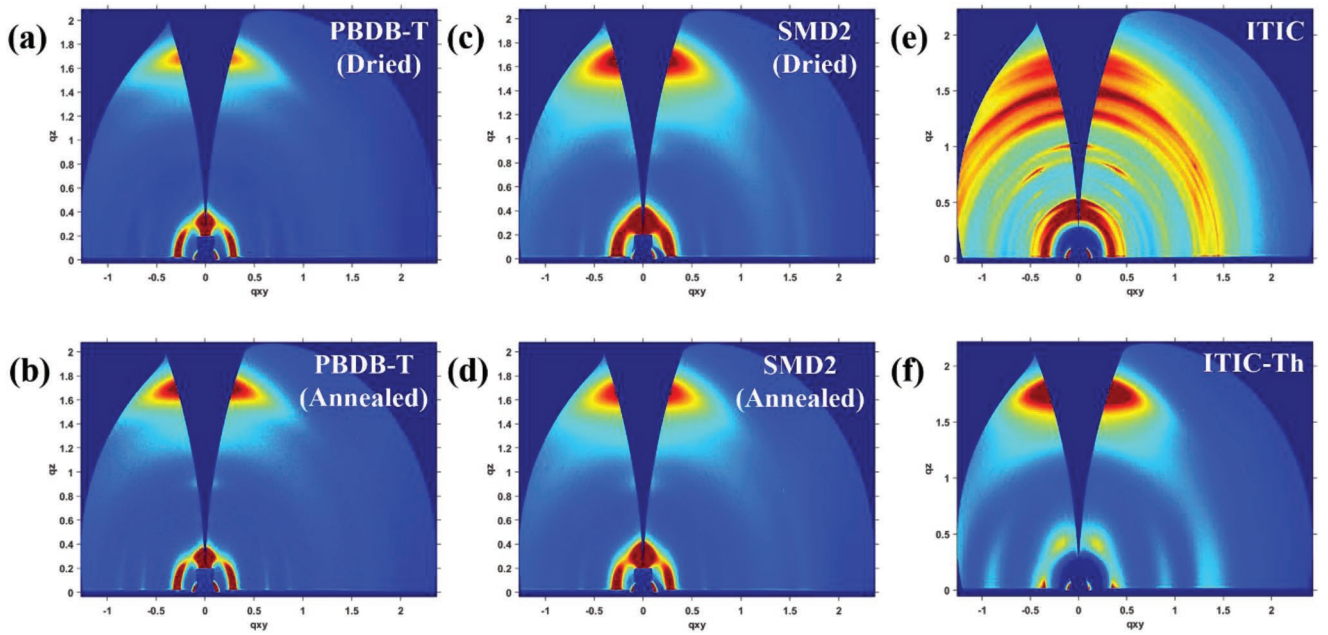

Figure 1. GIWAXS patterns for the pristine active materials. a) Dried and b) annealed films of PBDB-T; c) Dried and d) annealed films of SMD2; e) ITIC and f) ITIC-Th films.

in **Figure 1**. In particular, the donor polymers were analyzed in as-cast (dried) and annealed (160 °C) states with respect to the post-treatment, while the acceptors were analyzed in the annealed states at a mild temperature (100 °C) to drive the intrinsic crystallinity. The pristine photoactive materials were analyzed through line-cuts along the out-of-plane (OOP) and in-plane (IP) directions, and the lattice plane spacings were compared (Figure S9a–f and Table S2, Supporting Information). Using the integrated pole figure plots for the (100) lamellar diffraction of GIWAXS, the face-on and edge-on orientation proportions (A_{XY}/A_Z) of all the pristine materials were calculated (Figure S10 and Table S2, Supporting Information). Furthermore, crystal coherence lengths (CCLs) of the (100) and (010) stacking sizes in the OOP direction were calculated by the Scherrer equation, and the crystallinity was analyzed (Table S3, Supporting Information).[69]

The results showed that both donor polymers exhibited bimodal face-on and edge-on orientations with strong (100) and (010) diffraction peaks. However, the edge-on structures of SMD2 were two times larger than that of PBDB-T. First, PBDB-T showed (100), (200), and (300) peaks, exhibiting a regular increase in its crystallinity in a wide range and a decrease in its π–π stacking distance in the annealed state compared with the dried state (Figure S9a,b, Supporting Information). On the contrary, SMD2 exhibited a highly crystalline structure without any post-treatment (Figure S9c,d, Supporting Information). Moreover, the edge-on structures of SMD2 were two times larger than that of PBDB-T, according to the calculation from the integrated pole figure plots data (A_{XY}/A_Z) (Figure S10, Supporting Information). In addition, SMD2 showed a closed-packed structure due to a change in the lamellar packing distance with the (100) peak (distance of ≈2.1 Å) in the dried film without any post-treatment. This trend is consistent with the change in the CCLs corresponding to (100) and (010) planes. Although the PBDB-T crystallinity increased upon annealing, the SMD2 crystallinity increased following the drying process. Furthermore, as seen from the GIWAXS data, ITIC-Th had lower crystallinity than ITIC (Figure S9e,f, Supporting Information). ITIC-Th showed longer lamellar packing distance (d_{100}) and shorter π–π stacking distance (d_{010}) than ITIC (in Table S2 in the Supporting Information). Therefore, it was inferred that ITIC would be more compatible with PBDB-T, which has lower crystallinity, while ITIC-Th would be more compatible with SMD2, which has higher crystallinity.[23,46,56,70]

To compare the compatibility the donor polymer and NFA components, the surface tension (γ) was determined and calculated from the contact angles measured using two solvents, water (distilled water) and oil (diiodomethane, DIM) in each pristine film (Figure S11 and Table S4, Supporting Information). The blend miscibility was estimated using the Flory–Huggins interaction parameter (χ).[71–74] As a result, the calculated χ values for PBDB-T and SMD2 showed 0.574 to 0.821 for blended with ITIC, and 0.260 to 0.434 for blended with ITIC-Th. It means that the polymer blends with ITIC-Th have a more miscible due to a relatively low χ values compared to those of ITIC. A low χ value leads to a too high miscible for the blend films. The homogeneous phase with smaller interfacial area resulted too high miscible properties would hinder exciton dissociation at interface between donor and acceptor. However, a too high χ value implies a too pure phase and potentially severe phase segregation, which leads to quench morphology. Thus, to find a relative balanced miscibility of the polymer blends is very important to realize high performance OSCs.[75,76]

The miscibility variation was further investigated by performing DSC measurement (Figure S12, Supporting Information).[77] Both polymers already analyzed with amorphous nature in previous section. The pure NFAs of ITIC and ITIC-Th exhibit melting point temperatures (T_m) of 293.7 and 280.3 °C,

with melting enthalpies (ΔH_m) of 46.6 and 13.8 J g^{-1}, respectively. It is consistent with the results of GIWAXS that ITIC is more crystalline than ITIC-Th. After the polymers of PBDB-T and SMD2 were blended with ITIC, both polymer blends showed slightly decreased T_m and ΔH_m, respectively. It means that polymer blends with ITIC had a similar miscibility. However, PBDB-T:ITIC-Th showed largely decreased T_m and ΔH_m with 273.2 °C and 1.5 J g^{-1}, respectively, while SMD2:ITIC-Th showed unchanged T_m, only ΔH_m is slightly decreased to 7.8 J g^{-1}. These results indicate the molecular packing in the SMD2:ITIC-Th blend is more ordered than PBDB-T:ITIC-Th. Further estimating the molecular interaction parameter using the Nish–Wang equation, this value in the SMD2:ITIC-Th is more higher compared to PBDB-T:ITIC-Th according to value of $\Delta H_m/T_m$ term increased. Thus, SMD2:ITIC-Th will lead to high FF with high domain purity.[71,73,77]

According to comprehensively the GIWAXS, Flory–Huggins interaction, and DSC results, SMD2 showed a relative high crystallinity compared to PBDB-T, also, ITIC showed a much higher crystallinity than ITIC-Th. In addition, ITIC-Th blends are better than that of ITIC in aspect of miscibility. Therefore, the SMD2:ITIC-Th blend could be a reasonable combination with an optimal balance between crystallinity and miscibility via the drying process alone without any post-treatment among the polymer blends.

2.3. Photovoltaic Properties of SMD2-Based OSCs

PBDB-T and SMD2 were combined with ITIC and ITIC-Th and used as BHJ layers, which have appropriate miscibility and crystalline structures for manufacturing inverted structure unit cells (active area of 0.04 cm^2). The performances of cells were analyzed and the current density–voltage (*J–V*) characteristics are shown in **Figure 2** and **Table 2**. The PBDB-T:ITIC-based BHJ layer had a highly crystalline structure and showed a high performance with a PCE of 10.3% after post-treatment at 160 °C for 10 min.[45] SMD2 showed a maximum PCE of 11.3% when blended with ITIC-Th without any post-treatment, and also showed a higher short circuit current density (J_{SC}) and fill factor (FF) than PBDB-T (17.3 mA cm^{-2} and 72.6%, respectively). The performances of the devices fabricated with PBDB-T, SMD2 with respect to post-treatment are shown in Table S5 (Supporting Information). The manufactured cells were certified by Daegu Technopark Nanoconvergence Practical Application Center (NPAC) to have a PCE of 11.6% (Figure 2d). The batch-to-batch variation of SMD2 is evaluated under the optimized devices and controlled within PCE variation of ≈6.0% (Table S6, Supporting Information). Consequently, SMD2, the NFAs-based material, is suitable for the R2R manufacturing process for fabricating high-performance, high-stability OSC modules without any post-treatment. Furthermore, to apply all-solution R2R process through "ProcessOne," it is necessary to enhance of UV-stability of SMD2. Additionally, the light-soaking stabilities of the devices with PBDB-T and SMD2 were measured in an ambient atmosphere for 350 h with two types of lamps under 1 sun irradiation (light-soaking stabilities and spectral irradiances are shown in Figure 2e–h). Under a xenon lamp with a UV region, both devices exhibited a dramatic decrease in stability, whereas under a white light-emitting diode (LED) lamp without a UV region, the device with SMD2 exhibited a high stability of over 80%. These results mean that UV-stability still remains a problem to be solved.

We selected HTL Solar as modified-PEDOT:PSS, which can be introduced by the solution process, to apply SMD2 to flexible OSC modules. Based on the light-soaking stability, the WO_3 layer, as multifunctional HTLs, which could decrease UV-degradation during the electrode-forming screen printing process in module manufacturing, was introduced with HTL Solar and its properties were analyzed.

The schematic image of the photostability test process, and the *J–V* characteristics (pristine devices and after UV-exposure) of the unit cells manufactured by the solution process are shown in **Figure 3**; the corresponding performances are presented in **Table 3**. The devices were fabricated with inverted structures (ITO/ZnO/SMD2:ITIC-Th/HTLs/Ag) in ambient atmosphere. HTL Solar (Device 4) and WO_3/HTL Solar (Device 5) were used as a single HTL and bilayer HTLs, respectively. Device 3, which did not use HTLs, showed a low PCE of 1.2%. After the introduction of HTL Solar, Device 3 showed a maximum PCE of 7.9%. Due to the mismatch of energy level between the deep HOMO level of SMD2 and the energy level of HTL Solar, the V_{OC} of SMD2 was 0.1 V lower than that of the device fabricated with evaporated MoO_3 (with energy level of –5.3 eV).[51] The mismatch of energy level can be explained with lower V_{OC} of conventional structured device introduced HTL Solar in Table S7 (Supporting Information). In contrast, the incorporation of bilayer HTLs resulted in a maximum PCE of 10.3% (J_{SC} = 17.3 mA cm^{-2}, V_{OC} = 0.899 V, and FF = 66.0%) with enhancing J_{SC}, V_{OC}, and FF. The V_{OC} was higher than that of the device with only HTL Solar. In short, HTL Solar showed a high J_{SC}, while the WO_3 layer showed high V_{OC} (the thickness optimization performances of the HTLs are shown in Table S8 in the Supporting Information). Consequently, the simultaneous incorporation of WO_3 and HTL Solar decreased series resistance (R_S) (5.3 Ω cm^2) and increased shunt resistance (R_{SH}) (678.4 Ω cm^2). The conductivity properties of pristine HTLs are shown in Figure S13 (Supporting Information). The high conductivity properties with WO_3 layer (20 nm) in bilayer HTLs caused reduction of R_S and consequently contributed to a high PCE.

To analyze the photostability of the devices, they were exposed to a UV-exposure system (Figure 3a) and the performances of the manufactured devices were evaluated (detailed processes are shown in Figure 3b, and the performances of the devices fabricated through UV-exposure are shown in Figure 3d, (≈1600–1700 mJ cm^{-2} for 5 min)). Devices 3′ and 4′ showed marked decreases in V_{OC} and FF, which are due to the photodegradation of the BHJ layer under HTL Solar during UV-exposure. In contrast, Devices 5′ and 6′ showed excellent photostability overall, with a small decrease in FF only after UV-exposure. In Figure S14 (Supporting Information), Devices 3 and 4 showed decreased EQE intensity following UV-exposure, especially at λ = 300–800 nm due to the photo-oxidation resulted from the defects of the NFAs-based BHJ layer after UV-exposure.[46,57] On the other hand, Devices 5 and 6, which have WO_3 layers, showed high EQE characteristics following UV-exposure; only the short-wavelength region showed a small decrease. Compared with the devices manufactured in an inert

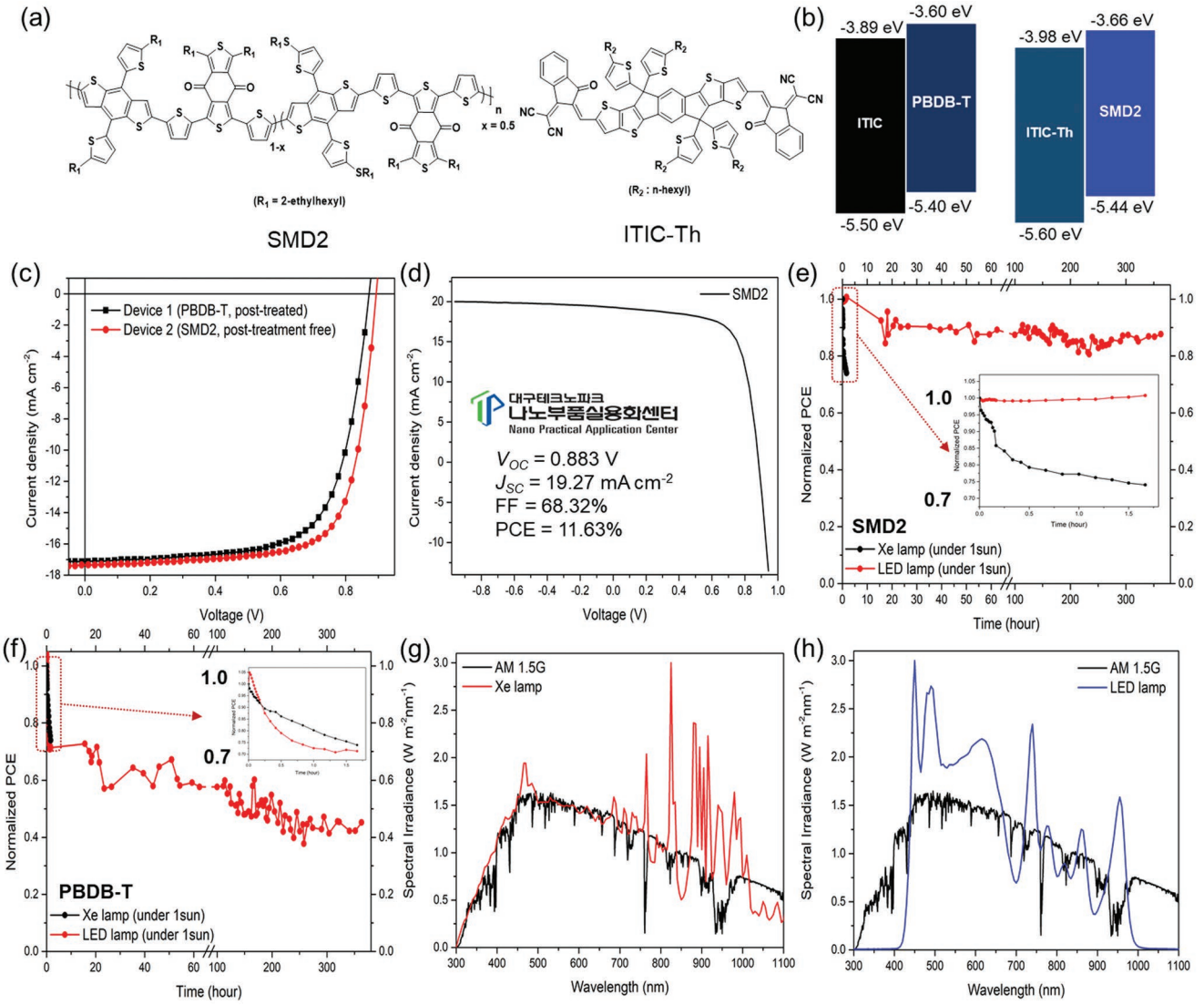

Figure 2. a) Chemical structures of SMD2, ITIC-Th introduced as BHJ layer, and b) energy level alignment of PBDB-T:ITIC and SMD2:ITIC-Th, and c) *J*–*V* characteristics of fabricated devices (unit cells with active area of 0.04 mm^2, MoO_3/Ag), d) certificated performance from Daegu Technopark Nano Practical Application Center (NPAC), e) normalized PCE data under 1 sun irradiation (light-soaking) by Xe lamp (black) and LED lamp (red) over 350 h of (e) SMD2 device without post-treatment process and f) PBDB-T device with post-treatment process (inset images are shown performances for initial 2 h), spectral irradiances with respect to light source g) Xe lamp, h) LED lamp versus AM 1.5G spectrum.

atmosphere, the devices manufactured in ambient atmosphere showed outstanding performances, thereby indicating that devices with a small V_{OC} drop and improved photostability could be manufactured independent of the atmosphere (performances of devices fabricated in inert atmosphere are shown in Figure S15 and Table S9, Supporting Information). Furthermore, devices fabricated with Ag paste and UV-curing process showed drastic changes due to morphological features

Table 2. Photovoltaic performances of fabricated devices based on PBDB-T and SMD2 with optimal process condition: Devices were fabricated with inverted structure (ITO/ZnO/BHJ layer/MoO_3/Ag, active area of 0.04 cm^2).

BHJ layer	Post-treatment	J_{SC} [mA cm^{-2}]	V_{OC} [V]	FF [%]	PCE_{max}[a)] [%]	R_{SH}[d)] [Ω cm^2]	R_S[d)] [Ω cm^2]
PBDB-T[b)]	Annealed (Device 1)	17.1	0.878	68.6	10.3	648	5.3
SMD2[c)]	Dried (Device 2)	17.3	0.899	72.6	11.3	753.2	4.3

[a)]The maximum value was obtained from best performance among fabricated devices; [b)]PBDB-T based devices exhibited best performance when composed with ITIC (annealing time was 10 min); [c)]SMD2 based devices exhibited best performance when composed with ITIC-Th (drying time was 10 min); [d)]R_{SH} and R_S were calculated in the equivalent circuit.

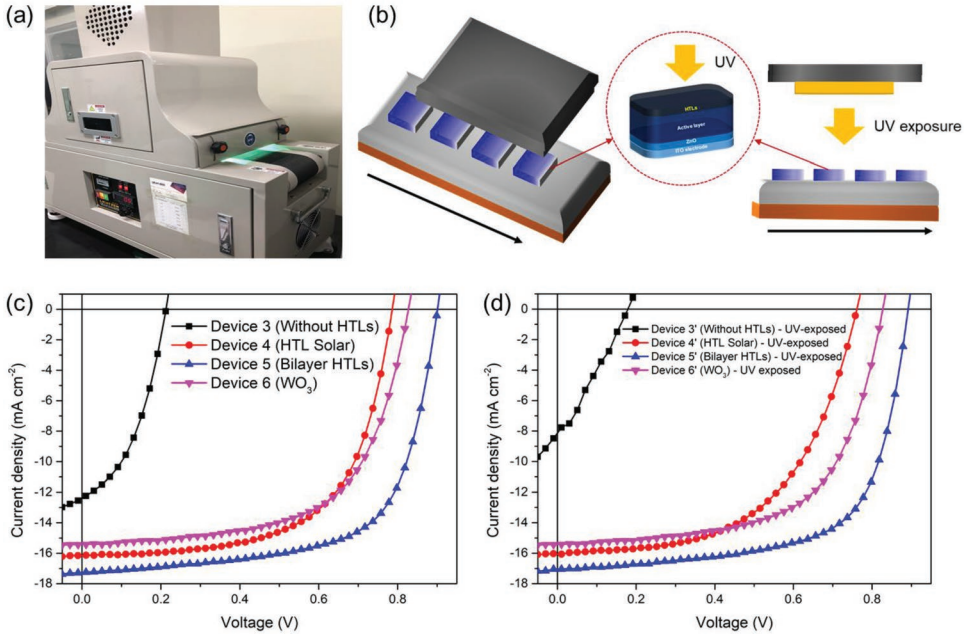

Figure 3. a) Actual image and b) schematic image of UV-exposure system for testing UV-stability of fabricated devices, and *J*–*V* characteristics of c) as fabricated devices and d) devices after UV-exposure (without Ag electrode).

(Table 3, Figure S16, Supporting Information). In these cases, device with only HTL Solar exhibited lower J_{SC}, V_{OC}, and FF due to rough surface with UV-degradation (In Figure S16c, Supporting Information). By means of introducing bilayer HTLs, the photovoltaic factors were all enhanced. Consequently, for matching internal potential and enhancing photostability against UV-curing process, the strategy introducing bilayer HTLs with WO_3 layer is essential for NFAs system with all-solution process.

2.4. Energy Level Matching and Internal Potential of HTLs

In the NFAs-based solution-processed OSCs, a strategy to reduce the mismatch of energy level between the deep HOMO level of SMD2 and the energy level of HTL Solar is necessary for V_{OC} recovery.[51] Particularly, the incorporation of HTLs that could match the energy level would help reduce the V_{OC} drop. **Figure 4** shows the energy level properties of the manufactured devices, internal potential with the light source, and J_{SC}, V_{OC}–light intensity (I) dependence properties. The analyses, as shown in Figure 4a–c, exhibit changes in the work function of the HTLs incorporated in the Ag electrode, $E_{cut\text{-}off}$, $E_{on\text{-}set}$, and energy level alignment with the BHJ layer, as determined by ultraviolet photoelectron spectroscopy (UPS) analysis.[78,79] The work functions were −4.74 eV for pristine Ag, −5.05 eV for HTL Solar/Ag, and −5.27 eV for bilayer HTLs/Ag. The pristine BHJ layer (−5.44 eV) and Ag formed a large hole-injection barrier (HIB, Ψ_h ≈0.7 eV) at the interface.[80,81] And these injection

Table 3. Photovoltaic performances of fabricated devices introduced with HTLs in ambient atmosphere: Devices were fabricated with inverted structure (ITO/ZnO/BHJ layer/HTLs/Ag, active area of 0.04 cm^2).

Device structure	Electrode	J_{SC} [mA cm^{-2}]	V_{OC} [V]	FF [%]	PCE_{max} [a] [%]	R_{SH} [d] [Ω cm^2]	R_S [d] [Ω cm^2]
Device 3 [b] (Without HTLs)	Ag	12.5	0.212	41.6	1.2	26.3	10.9
Device 4 [b] (HTL Solar)	Ag	16.1	0.777	62.6	7.9	410.7	7.1
Device 5 [b] (Bilayer HTLs)	Ag	17.3	0.899	66.0	10.3	678.4	5.3
Device 6 [b] (WO_3)	Ag	15.3	0.818	62.7	8.3	614.4	7.8
Device 3' [b] (after UV exposed)	Ag	8.5	0.171	27.4	0.399	22.1	15.2
Device 4' [b] (after UV exposed)	Ag	16.0	0.757	55.4	6.7	395.6	9.8
Device 5' [b] (after UV exposed)	Ag	17.1	0.899	65.0	10.0	562.4	6.1
Device 6' [b] (after UV exposed)	Ag	15.4	0.818	62.1	8.3	537.2	8.2
HTL Solar [c]	Ag paste	14.7	0.737	47.6	5.2	234.8	9.9
Bilayer HTLs [c]	Ag paste	15.1	0.858	61.9	8.0	497.2	7.2

[a]The maximum value was obtained from best performance among fabricated devices; [b]Devices were fabricated with Ag electrode formed via thermal evaporation; [c]Devices were fabricated with Ag paste and UV-curing process (≈1600 mJ cm^{-2} for 5 min); [d]R_{SH} and R_S were calculated in the equivalent circuit.

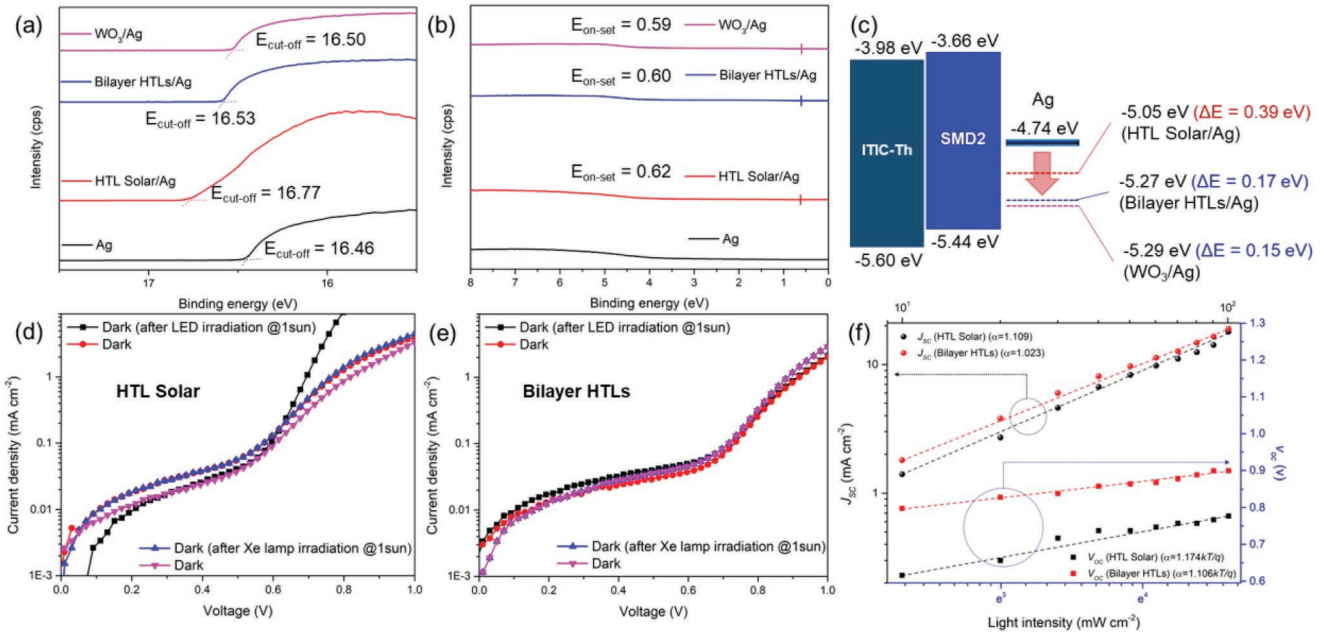

Figure 4. a) $E_{cut\text{-}off}$, b) $E_{on\text{-}set}$ characteristics calculated through UPS analysis of HTLs coated on Ag electrode, c) schematic image of energy level alignment and dark *J*–*V* characteristics of d) HTL Solar, e) bilayer HTLs with respect to measurement under different light source, f) J_{SC}, V_{OC}–light intensity dependence characteristics of fabricated devices introduced with HTL Solar and bilayer HTLs.

barriers can be reduced by effects of interfacial matching.[82] With the incorporation of HTL Solar, a HIB of $\Psi_h = 0.39$ eV was observed. A large HIB lowers the internal potential of the device and increases the V_{OC} drop and carrier recombination.[81,83]

In Figure 4d,e, the dark *J*–*V* characteristics of the devices are shown. The devices were pre-exposed during 30 min individually using a warm white LED lamp and Xe lamp, and then measured under Xe lamp at 1 sun (100 mW cm^{-2}) for analysis of internal potential shift. A LED lamp has a narrower wavelength than a Xe lamp, and a warm white LED shows emission properties at λ = 450–680 nm (shown in Figure 2g,h).[84,85] The devices containing only HTL Solar showed a marked difference in slopes when pre-exposed to the LED lamp and Xe lamp due to deficient internal potential with large HIB. Although only HTL Solar incorporated devices exhibited a decrease in HIB in the BHJ layer/Ag interfaces, a large difference between the donor HOMO level and HTL Solar caused a V_{OC} drop due to a low internal potential.[51,86] In contrast, the bilayer HTLs incorporated devices showed a small HIB of $\Psi_h = 0.17$ eV, and formed an ohmic contact through the well-matched energy level alignment. In addition, the devices with the bilayer HTLs exhibited dark *J*–*V* curves without change after white LED lamp and Xe lamp exposure resulted from enhanced internal potential. These well-matched energy level alignment is owing to an energetic cascade alignment of SMD2-WO_3-HTL Solar with the aid of a WO_3 layer, which recovered V_{OC} (0.899 V) (Figure S17, Supporting Information).

Figure 4f shows the J_{SC}, V_{OC}–light intensity (I) dependence characteristics of the devices containing HTL Solar and bilayer HTLs. Generally, J_{SC} shows a power-law relationship with I and V_{OC} exhibits the relationship $V_{OC} \propto kT/q\ln(I)$ with I, where k is the Boltzmann constant, T is the absolute temperature, and q denotes the elementary charge. For HTL Solar, α = 1.109 and slope = 1.174 kT/q, while for the bilayer HTLs, α = 1.023 and slope = 1.106 kT/q. Consequently, the incorporation of bilayer HTLs led to well-matched energy level alignment, which strengthened the internal potential and decreased carrier recombination resulting in decreased R_S and increased R_{SH}.[87,88]

Further, to confirm the improved carrier transport properties resulting from the incorporation of HTLs, the electron and hole mobility characteristics were analyzed (Figure S18 and Table S10, Supporting Information). The carrier mobility characteristics were based on the *J*–*V* characteristics measured using an electron-only device and a hole-only device and were calculated using the Mott–Gurney space charge limited current method. Compared with the devices containing only HTL Solar ($\mu_e = 2.09 \times 10^{-4}$ cm^2 V^{-1} s^{-1}, $\mu_h = 9.65 \times 10^{-5}$ cm^2 V^{-1} s^{-1}, μ_e/μ_h = 2.17), the devices containing bilayer HTLs ($\mu_e = 2.36 \times 10^{-4}$ cm^2 V^{-1} s^{-1}, $\mu_h = 1.68 \times 10^{-4}$ cm^2 V^{-1} s^{-1}, μ_e/μ_h = 1.41) showed high hole mobility and more balanced carrier transport properties. Consequently, the incorporation of bilayer HTLs led to improved J_{SC} and FF resulted from enhanced internal potential.

2.5. Photostability of HTLs

In this section, "photostability" means "photostability against UV-light during UV-curing process" for efficient transfer from small-area unit cells to large-area flexible OSC modules. The electric field distribution was calculated using finite-difference time domain (FDTD) analysis to investigate the photostability of HTL Solar and bilayer HTLs, and the results are shown in **Figure 5**,[89] along with the measured UV–vis absorption characteristics. In virtual space, HTL Solar and bilayer HTLs were incorporated into the devices with inverted structures on top

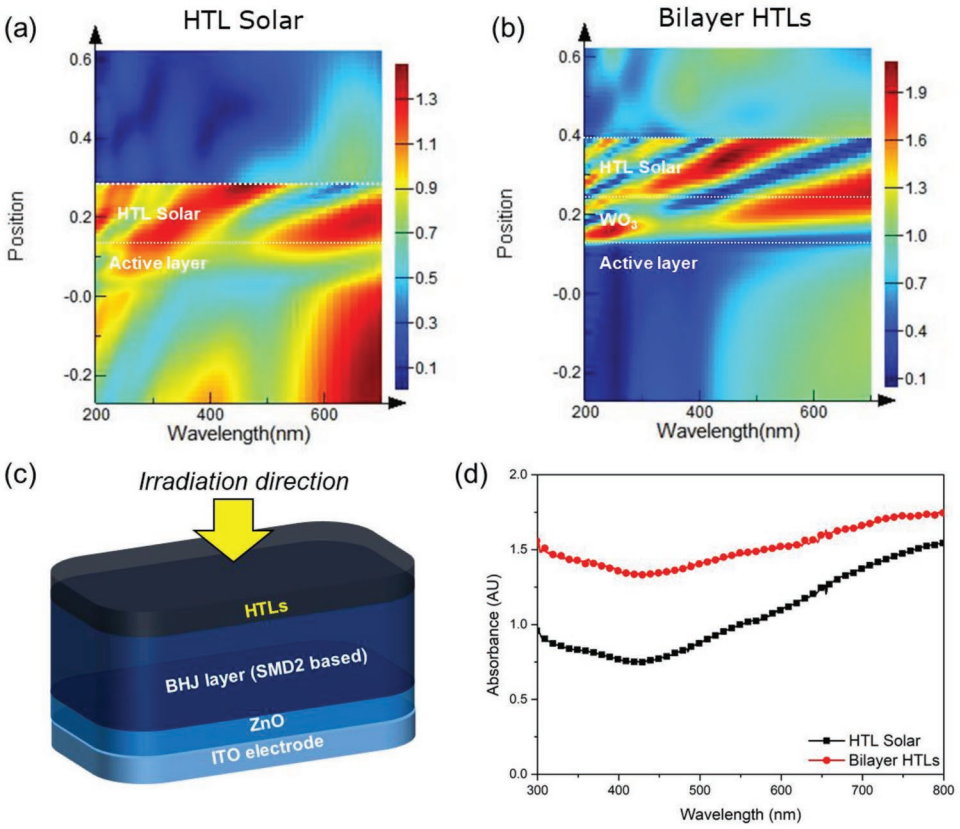

Figure 5. Optical simulation characteristics performed through FDTD solution of a) HTL Solar (single layer HTLs) and b) bilayer HTLs (red: optically high response region, blue: optically low response region, calculated with distributions of the electric field ($|E|$)), c) schematic image of UV–vis absorption characteristics of devices with respect to direction of source irradiation, d) absorption properties of HTLs measured based on ITO/ZnO/BHJ layer sample.

of the BHJ layer followed by exposure to a light source having the same intensity and range as solar irradiation. The FDTD analysis was performed using the same direction and method of exposure as that used for UV-curing in the screen printing process for the top Ag electrode in "ProcessOne." In the devices in which only HTL Solar was incorporated (Figure 5a), the irradiated light from the top of the PEDOT:PSS layer showed high response (in red region) to short-wavelength in the entire device (both of HTL Solar and BHJ layer) resulting in photodegradation of BHJ layer. Most of the incident light was transmitted through the BHJ layer in the devices in which only HTL Solar was incorporated.

In contrast, the bilayer HTLs devices (Figure 5b) showed high response to the short-wavelength region in only HTL Solar and WO_3 layers, whereas they showed a low response (blue region) to the short-wavelength region in the BHJ layer. In other words, most of the incident light was absorbed by the bilayer HTLs (especially the WO_3 layer) and did not reach the BHJ layer. This is due to the high absorption properties of the WO_3 layer in the short wavelength region.[60] Also, Figure S19 (Supporting Information) shows the schematic images of the detailed FDTD simulation analysis of the layer positions of the HTLs devices. The electric field distributions and transmittances at positions 1, 2, and 3 were determined by analyzing the light irradiated from the top to the bottom of the fabricated devices. Only the HTL Solar device showed a high response to the short wavelength region regardless of position (shown in Figure S19-1–S19-3, Supporting Information). During this process, photodegradation occurred in the NFAs-based BHJ layer due to direct UV-exposure.[57,58] In contrast, in the bilayer HTLs devices, At the point where the light passed position 2 (interface of WO_3 layer and BHJ layer), a markedly decreased response and transmittance in the short wavelength region was observed (shown in Figure S19-4–S19-7, Supporting Information). This is because the WO_3 layer absorbed the short-wavelength light (λ_{abs} = ≈335 nm, shown in Figure S20, Supporting Information). Therefore, the incorporation of WO_3 layer effectively improved the photostability of the fabricated devices.

Figure 5c,d shows the structures of samples for UV–vis absorption and measured absorption properties of the HTLs based on film of ITO/ZnO/BHJ layer blank. These confirmed the absorption of light that passed through the HTLs. The incorporation of bilayer HTLs contributed to relative higher absorption properties in the short-wavelength region, compared with only HTL Solar incorporated devices. These properties are consistent with the transmittance trends calculated for the interface of the HTLs and BHJ layer (Position 2) and indicate increased photostability owing to the incorporation of WO_3 layer. Consequently, unlike HTL Solar, which showed a larger decrease in J_{SC}, V_{OC}, and FF following UV-exposure, the

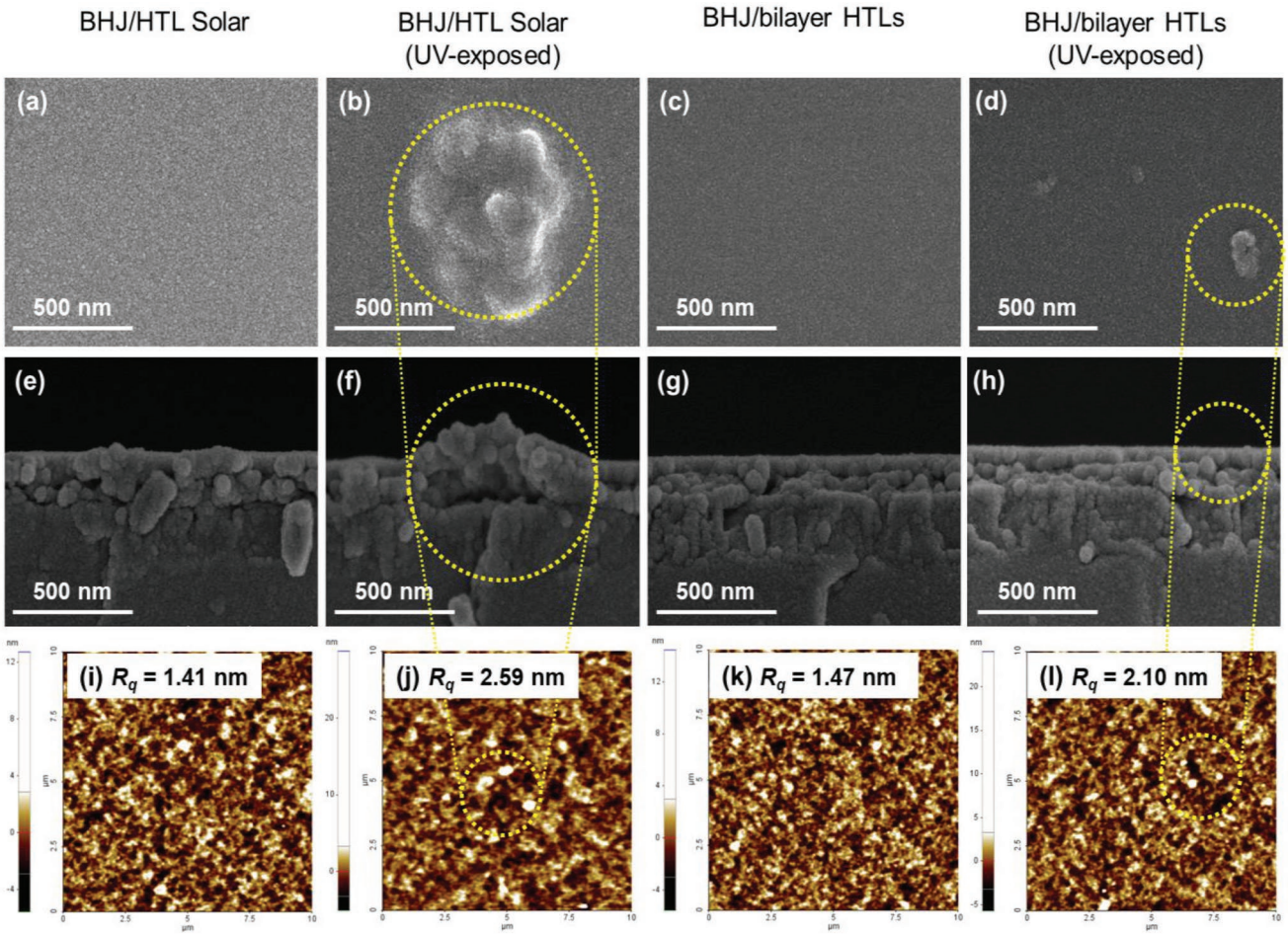

Figure 6. Top-view images of FE-SEM characteristics a–d), cross-sectional images of FE-SEM characteristics e–h), and morphology characteristics i–l) in order of BHJ/HTL Solar film, BHJ/HTL Solar film after UV-exposed, BHJ/bilayer HTLs film, and BHJ/bilayer HTLs film after UV-exposed.

incorporation of bilayer HTLs led to enhanced photostability that can stably maintain the photovoltaic properties.

2.6. Nanostructure and Morphology Characteristics

Figure S21 (Supporting Information) shows the surface XPS spectra of the HTL Solar and bilayer HTLs devices. Both HTL Solar and bilayer HTLs devices showed two sulfur (S) 2p peaks at 163.9 eV (S $2p_{3/2}$) and 165.1 eV (S $2p_{1/2}$) arising from the thiophene unit in PEDOT, and a peak at 168.8 eV (S $2p_{3/2}$ and S $2p_{1/2}$) arising from PSS.[90,91] In bilayer HTLs film, the PEDOT molecules introduced above the WO_3 layer resulted in high packing characteristics (enhanced intensity of PEDOT peak), which yielded enhanced electrical conductivity.[92] In the UV-exposed HTL Solar, oxidation and decomposition of PSS is generally observed;[90] however, the decrease in the PSS peak intensity for the bilayer HTLs was smaller than that for the only HTL Solar incorporated films. Figure S22 (Supporting Information) shows the water contact angles and surface energies of the BHJ layer and HTL films. Generally, interfaces of materials with similar surface energy can form a good contact.[93] Therefore, the incorporation of WO_3 layer, which has a surface energy of 31.06 mW m^{-1}, between the BHJ layer (10.54 mW m^{-1}) and HTL Solar (61.87 mW m^{-1}) resulted in the formation of a well-matched interfacial contact and removed the interfacial defects.[56] In the case where HTL Solar is incorporated above the BHJ layer in the inverted structure, many challenges with regard to surface properties and potential of interface instability need to be overcome.[94] Also, the introduction of bilayer HTLs led drastic decrease of $C–N^+$ peaks (400.6 eV) preventing the partial protonation of C–N functional groups in ITIC-Th against UV-exposure (information of N 1s and W 4f peaks are explained in Figure S21c,d, Supporting Information).[95] Consequently, the incorporation of WO_3 layer improved interfacial matching in BHJ layer/WO_3/HTL Solar compared with BHJ layer/HTL Solar, which led to compact stacking of PEDOT molecules resulting in high conductivity with low R_S and photostability. The surface XPS characteristics of BHJ layer, BHJ/WO_3 film and XPS depth-profiling characteristics of BHJ/HTLs films with or without UV-exposure are explained in Figures S23 and S24, Table S11 in the Supporting Information.

Figure 6 shows the morphological characteristics investigated using field emission-scanning electron microscopy (FE-SEM) and atomic force microscopy (AFM). The BHJ/HTL Solar film

showed a relatively uniform morphology at initial, and then formed large damaged surface after UV-exposure (RMS roughness, R_q changed from 1.41 to 2.59 nm). In contrast, although the BHJ/bilayer HTLs film initially showed uniform morphology, small damaged surface was formed after UV-exposure (R_q changed from 1.47 to 2.10 nm). These results are consistent with the morphological characteristics of pristine BHJ and BHJ/WO_3 films shown in Figure S25 (Supporting Information), which indicate that the incorporation of a WO_3 layer improved the photostability by preventing damaged surface on the BHJ layer due to UV-exposure. For Device 6 in which a WO_3 layer was incorporated, the V_{OC} improved due to energy level matching (with HIB of 0.15 eV), however, the V_{OC} was rather lower than bilayer HTLs. The lower performances of Device 6 were due to the increase in R_S resulting from the WO_3 layer surface voids acting as carrier recombination centers (Figure S25c,d, Supporting Information). After incorporating bilayer HTLs, devices exhibited not only high UV-stability, but also enhanced performances by forming perfectly covered surface.

GIWAXS analysis was performed to investigate the molecular packing and crystalline structure after incorporation of HTLs (Figure S26, Supporting Information). The detailed crystallographic characteristics are presented in Tables S12, and S13 (Supporting Information). The crystalline structure of the BHJ/HTLs film was similar to that of the pristine BHJ layer (GIWAXS images of pristine BHJ and UV-exposed pristine BHJ films are shown in Figure S27, Supporting Information). Ring-like peaks were observed at q_z = 1.3–1.5 Å^{-1} due to amorphous aggregation of PSS, and (010) peaks were observed at q_z = 1.7 Å^{-1} due to molecular stacking of BHJ and PEDOT.[96] Sharp and ordered (100) peaks (q_z = 0.33 Å^{-1}, d_{100} = 19.0 Å) were detected at the out-of-plane direction of bilayer HTLs film, which indicated a more well-ordered and close-packed crystalline structure than the HTL Solar (q_z = 0.31 Å^{-1}, d_{100} = 20.3 Å) film. With the incorporation of bilayer HTLs, the intensity of the PEDOT (010) peak (q_z = 1.73 Å^{-1}) increased and the π–π distance decreased. These results are attributed to the improved interfacial matching and enhanced conductivity owing to the incorporation of WO_3. Similar to the UV-exposed BHJ film (Figure S27b, Supporting Information), all the peak intensities of the HTL Solar film decreased due to UV-degradation. In the bilayer HTLs film, the decreases in peak intensities were relatively smaller and larger grains of irreversible sizes were formed after UV-exposure (Table S13, Supporting Information). Consequently, well-ordered molecular stacking owing to the incorporation of bilayer HTLs resulted in improved crystallinity and efficient carrier transport.

2.7. Evaporation-Free Flexible OSC Modules

In order to resolve mismatch of energy level and improve photostability, bilayer HTLs were incorporated to manufacture flexible OSC modules with inverted structures in an industrial production line (**Figure 7** and **Table 4**). All layers were formed by a slot-die coating method, and the top Ag electrode was formed by the screen printing method via a UV-curing process (≈5500 mJ cm^{-2}) for 2 min. Overall, flexible OSC modules comprising 10 cells connected in series were manufactured by the "ProcessOne" method,[30,31] which is an evaporation-free (all-solution) process and has high productivity. Modules in which only HTL Solar was incorporated showed a PCE of 2.02% (J_{SC} = 0.97 mA cm^{-2}, V_{OC} = 7.76 V, and FF = 26.7%) while the bilayer HTLs incorporated modules showed a maximum PCE of 5.25% (J_{SC} = 1.12 mA cm^{-2}, V_{OC} = 8.80 V, and FF = 53.1%), which is over two times that of the PEDOT:PSS modules. The low J_{SC}, V_{OC}, and FF of modules incorporated only HTL Solar was because of UV-degradation similar with unit cells introducing Ag paste electrode (Table 3). Although the SMD2:ITIC-Th-based modules showed uniform performance independent of the slot-die coated film location (Figure S28 and Table S14, Supporting Information), the maximum performances were achieved for the SMD2:ITIC-based modules with uniformity regardless of the slot-die coated film location (Figure 7c,d, Supporting Information). The thickness of BHJ layer in OSC modules formed via slot-die coating was optimized at 200 nm with lower thickness insensitive properties of SMD2:ITIC composition (Table S15, Supporting Information). Also, fabricated flexible OSC modules with bilayer HTLs exhibited high stability during 143 h under damp heat stress (85% relative humidity at 65 °C) without encapsulation (PCE was 4.44% which reduced ≈15% drop from initial state) (shown in Figure S29, Supporting Information). In addition, the incorporation of bilayer HTLs helped achieve an output performance of P_{max} = 419.6 mW, which is about 2.6 times larger than that of HTL Solar (P_{max} = 161.8 mW) and higher than that of the FAs-based modules (P_{max} = 373.0 mW; detailed performances were shown in Table S16, Supporting Information).

The geometric fill factor (GFF) is defined as ratio of active are to total area including interconnection region. The GFF of fabricated flexible solar module was 74.7% with each interconnection region of 2.1 mm for whole active layer of 80 cm^2. Ideally, the GFF should be large to suppress loss of PCE. According to electrical simulation performed by Brabec and co-workers, interconnection region over 0.5 mm would lead loss of PCE more than 50%.[97] The performance transfer between PCE_{cell} = 10.3% and PCE_{module} = 5.25% (the efficiency loss of 50.9%) is meaningful especially in NFAs-based evaporation-free modules with large area over 80 cm^2.

Consequently, the incorporation of bilayer HTLs, which imparted a high V_{OC} to the NFAs-based OSCs, enabled successful manufacturing of evaporation-free flexible OSC modules, which had higher power generation properties than FAs-based modules. Also, with these efforts, EPBT will effectively be reduced from 360 to 296.9 days with cost down of ≈$ 500 per meter.[98] The results of this study can be extended to realize high-performance NFAs-based modules and for manufacturing high-performance flexible modules by using an evaporation-free all-solution process, thus overcoming one of the serious obstacles to commercialization. With these advantages, the evaporation-free flexible OSC modules have unlimited potential for mass production of flexible devices and application in wearable devices.

3. Conclusion

In this study, NFAs-based BHJ materials and multifunctional bilayer HTLs, which overcome the challenges in the

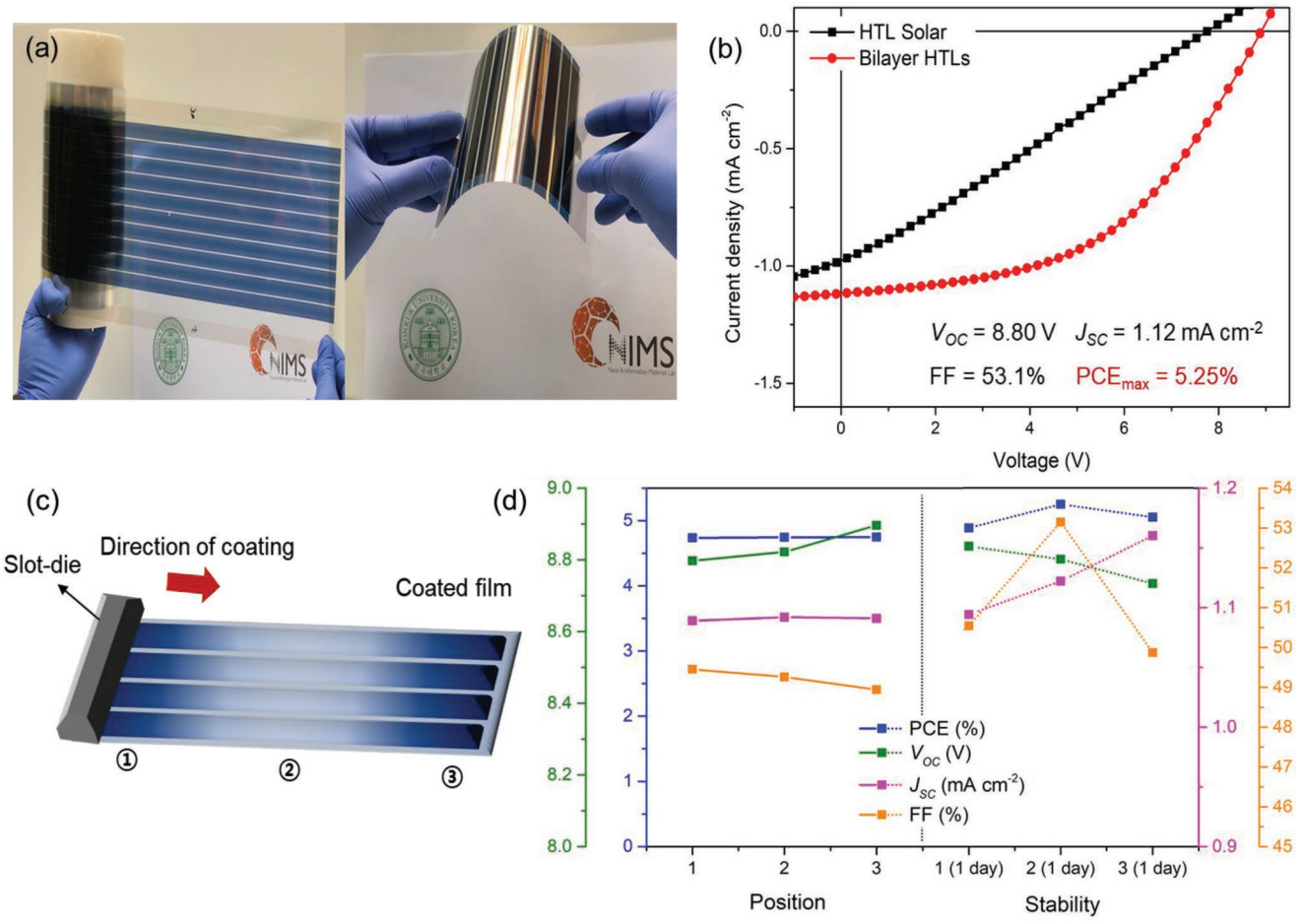

Figure 7. a) Images of fabricated evaporation-free flexible OSC modules (SMD2:ITIC based BHJ layer) and b) *J–V* characteristics of fabricated flexible OSCs introduced with HTL Solar and bilayer HTLs, c) schematic images of fabricated flexible OSC modules and locations (position of 1–3) divided according to direction of coating, d) photovoltaic factors measured at each location.

manufacturing of high-performance flexible OSC modules, were developed. By developing a donor polymer SMD2, which allows the utilization of a post-treatment-free process, a maximum PCE of 11.3% was achieved owing to the balanced miscibility and crystallinity realized with the combination of NFAs. To resolve the issues of V_{OC} drop and photodegradation, which are the challenges that arise during modulation of NFAs-based BHJ layer by using the all-solution process, bilayer HTLs structure was developed. With the incorporation of bilayer HTLs in WO_3/HTL Solar, the V_{OC} was effectively recovered through the formation of a high internal potential and energy level matching and the BHJ layer was successfully protected from UV-irradiation, which led to improved photostability of the devices. The maximum PCE of 10.3% was achieved incorporating bilayer HTLs in unit cells. Using these two strategies, flexible OSC modules were manufactured in industrial production lines by using evaporation-free and all-solution process, and a PCE of 5.25% and power output of 419.6 mW were achieved, which are higher than those of previous FAs-based flexible OSC modules (373.0 mW). Hence, a paradigm shifts from FAs-based flexible OSC modules to NFAs-based systems can be suggested. Furthermore, since the modules can be manufactured using an evaporation-free process, they can be produced at a low cost at the industrial scale as well as laboratory-scale. These high-performance modules have unlimited potential as an energy source that can be applied in various fields.

Table 4. Photovoltaic performances of fabricated evaporation-free flexible OSC modules: Modules were fabricated with inverted structure (ITO/ZnO/BHJ layer/HTLs/Ag(Ag paste formed screen printing and UV-curing), active area of 80 cm^2).

Device structure	J_{SC} [mA cm^{-2}]	V_{OC} [V]	FF [%]	PCE_{max} [a)] [%]	P_{max} [b)] [mW]	R_{SH} [c)] [Ω cm^2]	R_S [c)] [Ω cm^2]
HTL Solar	0.97	7.76	26.7	2.02	161.8	160.2	98.9
Bilayer HTLs	1.12	8.80	53.1	5.25	419.6	778.8	26.6

[a)]The maximum value was obtained from best performance among fabricated modules; [b)]The maximum power was calculated by J_{max} and V_{max}; [c)]R_{SH} and R_S were calculated in the equivalent circuit.

4. Experimental Section

Materials for SMD2: The detailed synthetic procedures and characterization for SMD2 are provided in the Supporting Information (Scheme S1 and Figures S1–S3, Supporting Information). All the reactions were carried out under an inert N_2 atmosphere. All reagents and chemicals were purchased from commercial sources (Aldrich and Acros) and used without further purification unless stated otherwise. 1,3-Bis(5-bromothiophen-2-yl)-5,7-bis(2-ethylhexyl)benzo[1,2-c:4,5-c′]dithiophene-4,8-dione (DTBDD-Br, A1) was synthesized and characterized according to the details given in a previous study.[41] 1,3-Dibromo-5,7-bis(2-ethylhexyl)benzo[1,2-c:4,5-c′]-dithiophene-4,8-dione (BDD), 4,8-Bis[5-(2-ethylhexyl)thiophen-2-yl]-2,6-bis(trimethylstannyl)benzo[1,2-b:4,5-b′]dithiophene (D1), and 4,8-bis(5-((2-ethylhexyl)thio)thiophen-2-yl)benzo[1,2-b:4,5-b′]-dithiophene-2,6-iyl)bis(trimethylstannane) (D2) were obtained from Sunatech and Solarmer Inc. Nonfullerene acceptors for 3,9-bis(2-methylene-(3-(1,1-dicyanomethylene)-indanone))-5,5-11,11-tetrakis(4-hexylthienyl)-dithieno[2,3-d:2′,3′-d′]-s-indaceno[1,2-b:4,5-b′]dithiophene (ITIC-Th) and 2,2′-[[6,6,12,12-Tetrakis(4-hexylphenyl)-6,12-dihydrodithieno[2,3-d:2′,3′-d′]-s-indaceno[1,2-b:5,6-b′]dithiophene-2,8-diyl]bis[methylidyne(3-oxo-1H-indene-2,1(3H)-diylidene)]] bispropanedinitrile (ITIC) were obtained from Derthon Inc. The commercialized donor polymer PBDB-T was purchased from 1-Materials, characterized, and then compared to SMD2.

Materials for Fabricating Organic Solar Cells: SMD2 was synthesized following procedures in Scheme S1 (Supporting Information). The PBDB-T used as donor for comparison with SMD2 was purchased from 1-Materials (Canada). The ITIC-Th and ITIC used as acceptors were purchased from 1-Materials (Canada) and Solarmer (USA), respectively. The chlorobenzene (CB) and 1,8-diiodooctane (DIO) used as a solvent and additives were purchased from Sigma-Aldrich (Germany). Zinc acetate dehydrate [$Zn(CH_3COO)_2 \cdot 2H_2O$], ethanolamine, and 2-methoxyethanol (used as precursors for the ZnO) were purchased from Sigma-Aldrich (USA). HTL Solar (Clevios HTL Solar, PEDOT:PSS) used as the HTLs was purchased from Heraeus (Germany). The Indium tin oxide (ITO) glass (sheet resistance of 10 Ω sq^{-1}) used as the electrode for the OSCs was purchased from AMG (Republic of Korea).

Fabrication of OSCs with Unit Cells (1) Evaporation Type, 2) Solution Process Type): To fabricate the OSCs, patterned ITO glass was cleaned via ultra-sonication in a wet cleaning process using a neutral detergent, isopropyl alcohol, and deionized water. The cleaned ITO glasses were treated with UV–ozone (UVO) in a UVO cleaner (Ahtech LTS). The devices were fabricated with an inverted structure (ITO/ZnO/BHJ layer/HTLs/Ag). The ZnO precursors introduced as ETLs were spin-coated onto the cleaned ITO glasses at 3000 rpm and annealed at 150 °C for 1 h. Three types of BHJ layers formed with PBDB-T:ITIC in a ratio of 1:1 (20 mg mL^{-1}) and with SMD2:ITIC-Th and SMD2:ITIC at a ratio of 1:1 (15 mg mL^{-1}). 1) To compare PBDB-T and SMD2, MoO_3 was introduced as HTLs via a thermal evaporation process. 2) To fabricate solution-processed devices, the WO_3 used as multifunctional HTLs (WO_3/HTL Solar bilayer structure) was coated via hydrolytic conversion from tungsten ethoxide in isopropyl alcohol (IPA, Sigma Aldrich) (1–2 mg mL^{-1}) with stirring for overnight in ambient atmosphere, and then the films stored in same atmosphere.[59–62] Finally, the top Ag electrode was formed via a thermal evaporation process in a vacuum chamber (under 1×10^{-7} torr) or screen printing with Ag paste which was dried in a UV-curing system (≈1600 mJ cm^{-2}) for 5 min. The total active area was 0.04 cm^2.

Fabrication of All-Solution Processed Flexible OSC Modules (3) All-Solution Process): 3) The flexible OSC modules were fabricated on a production line at the KOLON Advanced Research Cluster (Republic of Korea) through research collaboration accordance with method of "ProcessOne." All processes of fabricating flexible OSC modules were conducted in ambient atmosphere. To fabricate flexible OSC modules with inverted structure, all of buffer layer and BHJ layer were coated in optimal thickness via a slot-die coating process using commercial R2R coater without any pre-/post- treatment. For slot-die coating of ZnO layer, stock solution of ZnO nanoparticles (average sizes of 5 nm in mixed alcohol of butanol and IPA, 1-Materials) were prepared. The ZnO nanoparticles introduced as ETLs were formed via slot-die coating process (typical coating speed of 0.5 m min^{-1}, feed rate of 0.2 m min^{-1}) on a patterned ITO-polyethylene terephthalate (PET) film. The BHJ layers that formed with SMD2 and each of the ITIC and ITIC-Th (BHJ solution was prepared as same manner with unit cells, thickness was up to 200 nm). Also, for reference flexible OSC modules, BHJ solution consisted with PV-D4610 and A700 (Merck KGaA) were prepared as FAs-based system. The BHJ layers were coated via the slot-die coating process onto a coated ZnO layer (typical coating speed of 0.3 m min^{-1}, feed rate of 0.3 m min^{-1}). WO_3 stock solution prepared via hydrolytic conversion from tungsten ethoxide in IPA (Sigma Aldrich, 1–2 mg mL^{-1}) with stirring for overnight in ambient atmosphere.[59–62] For the bilayer HTLs, the WO_3 layer was formed via a slot-die coating process (typical coating speed of 0.5 m min^{-1}, feed rate of 0.3 m min^{-1}). The HTL Solar (Clevios HTL Solar, Heraeus) were formed via slot-die coating onto a coated WO_3 or BHJ layer (typical coating speed of 1.0 m min^{-1}, feed rate of 0.3 m min^{-1}). Finally, the top Ag electrode was formed via screen printing (Daeyoung-tech.) with Ag paste (opaque, Toyo-tech.) which was then dried in a UV-curing system (≈5500 mJ cm^{-2}) for 2 min. Consequently, the 10 individual cells were series connected forming total active area of 80 cm^2.

Characterization of Fabricated Devices: The current density–voltage (*J–V*) characteristics and current density, voltage–light intensity dependence characteristics of fabricated OSCs were performed with a power source meter (Keithley 2400) and a solar simulator (Oriel, AM1.5G under a 100 mW cm^{-2} illumination with Xe and LED lamps). The external quantum efficiency (EQE) was characterized with an incident power conversion efficiency (IPCE) measurement system (Mc science, Polaronix K3100). The photostability of devices fabricated via the solution process was verified with a UV-exposure machine (Lichtzen, 1600–1700 mJ cm^{-2} for unit cells). The ultraviolet photoelectron spectroscopy analysis was performed with AXIS-NOVA (Kratos). Optical simulation characteristics were determined using finite-difference time-domain solution software (Lumerical). The absorption characteristics of HTLs and the BHJ layer were analyzed with an ultraviolet–visible (UV–vis) spectrometer (Agilent 8453). XPS surface and depth profiling analyses were performed with an ULVAC-PHI 5000 VersaProbe (ULVAC). The contact angle and surface energy characteristics were measured with a contact angle analyzer (DSA100, KRUSS). The field emission scanning electron microscope analysis was performed with a SU8010 (Hitachi). The atomic force microscopy analysis was performed with a PSIA XE-100 (Park Systems). The grazing-incidence wide-angle X-ray scattering analyses were performed with the 3C beamline at the Pohang Accelerator Laboratory (PAL).

Supporting Information

Supporting Information is available from the Wiley Online Library or from the author.

Acknowledgements

Y.W.H. and S.J.J. contributed equally to this work. This research was supported by New & Renewable Energy Core Technology Program of the Korea Institute of Energy Technology Evaluation and Planning(KETEP) grant funded by the Ministry of Trade, Industry and Energy(MOTIE) of the Republic of Korea (Grant no. 20153010140030 and grant no. 2018201010636A) and the Human Resources Program in Energy Technology of the Korea Institute of Energy Technology Evaluation and Planning(KETEP) grant funded by the Ministry of Trade, Industry and Energy(MOTIE) of the Republic of Korea (Grant no. 20194010201790).

Conflict of Interest

The authors declare no conflict of interest.

Keywords

all-solution process, large area device, nonfullerene, organic solar cell modules, roll-to-roll process

Received: June 27, 2019
Revised: August 31, 2019
Published online:

[1] R. Sun, J. Guo, C. Sun, T. Wang, Z. Luo, Z. Zhang, X. Jiao, W. Tang, C. Yang, Y. Li, J. Min, *Energy Environ. Sci.* **2019**, *12*, 384.
[2] T. Lei, R. Peng, W. Song, L. Hong, J. Huang, N. Fei, Z. Ge, *J. Mater. Chem. A* **2019**, *7*, 3737.
[3] W. Song, X. Fan, B. Xu, F. Yan, H. Cui, Q. Wei, R. Peng, L. Hong, J. Huang, Z. Ge, *Adv. Mater.* **2018**, *30*, 1800075.
[4] Y. Lin, Y. Jin, S. Dong, W. Zheng, J. Yang, A. Liu, F. Liu, Y. Jiang, T. P. Russell, F. Zhang, F. Huang, L. Hou, *Adv. Energy Mater.* **2018**, *8*, 1701942.
[5] Q. Kang, B. Yang, Y. Xu, B. Xu, J. Hou, *Adv. Mater.* **2018**, *30*, 1801718.
[6] L. Meng, Y. Zhang, X. Wan, C. Li, X. Zhang, Y. Wang, X. Ke, Z. Xiao, L. Ding, R. Xia, H.-L. Yip, Y. Cao, Y. Chen, *Science* **2018**, *361*, 1094.
[7] S. Li, L. Ye, W. Zhao, H. Yan, B. Yang, D. Liu, W. Li, H. Ade, J. Hou, *J. Am. Chem. Soc.* **2018**, *140*, 7159.
[8] W. Li, L. Ye, S. Li, H. Yao, H. Ade, J. Hou, *Adv. Mater.* **2018**, *30*, 1707170.
[9] H. Yao, F. Bai, H. Hu, L. Arunagiri, J. Zhang, Y. Chen, H. Yu, S. Chen, T. Liu, J. Y. L. Lai, Y. Zou, H. Ade, H. Yan, *ACS Energy Lett.* **2019**, *4*, 417.
[10] H. Li, Z. Xiao, L. Ding, J. Wang, *Sci. Bull.* **2018**, *63*, 340.
[11] M. Zhang, R. Ming, W. Gao, Q. An, X. Ma, Z. Hu, C. Yang, F. Zhang, *Nano Energy* **2019**, *59*, 58.
[12] B. Yang, S. Zhang, S. Li, H. Yao, W. Li, J. Hou, *Adv. Mater.* **2019**, *31*, 1804657.
[13] S. Xiong, L. Hu, L. Hu, L. Sun, F. Qin, X. Liu, M. Fahlman, Y. Zhou, *Adv. Mater.* **2019**, *31*, 1806616.
[14] Q. Kang, L. Ye, B. Xu, C. An, S. J. Stuard, S. Zhang, H. Yao, H. Ade, J. Hou, *Joule* **2019**, *3*, 227.
[15] G. Liu, J. Jia, K. Zhang, X. Jia, Q. Yin, W. Zhong, L. Li, F. Huang, Y. Cao, *Adv. Energy Mater.* **2019**, *9*, 1803657.
[16] Y. Zhao, G. Wang, Y. Wang, T. Xiao, M. A. Adil, G. Lu, J. Zhang, Z. Wei, *Sol. RRL* **2019**, *3*, 1800333.
[17] E. G. Jeong, Y. Jeon, S. H. Cho, K. C. Choi, *Energy Environ. Sci.* **2019**, *12*, 1878.
[18] Y. Li, S. Arumugam, C. Krishnan, M. D. B. Charlton, S. P. Beeby, *ChemistrySelect* **2019**, *4*, 407.
[19] J. Zhang, G. Xu, F. Tao, G. Zeng, M. Zhang, *Adv. Mater.* **2019**, *31*, 1807159.
[20] Q. Tai, F. Yan, *Adv. Mater.* **2017**, *29*, 1700192.
[21] W. Zhao, S. Zhang, Y. Zhang, S. Li, X. Liu, C. He, Z. Zheng, J. Hou, *Adv. Mater.* **2018**, *30*, 1704837.
[22] S. Badgujar, G. Y. Lee, T. Park, C. E. Song, S. Park, S. Oh, W. S. Shin, S. J. Moon, J. C. Lee, S. K. Lee, *Adv. Energy Mater.* **2016**, *6*, 1600228.
[23] T. Zhang, G. Zeng, F. Ye, X. Zhao, X. Yang, *Adv. Energy Mater.* **2018**, *8*, 1801387.
[24] S. Hong, H. Kang, G. Kim, S. Lee, S. Kim, J. H. Lee, J. Lee, M. Yi, J. Kim, H. Back, J. R. Kim, K. Lee, *Nat. Commun.* **2016**, *7*, 10279.
[25] Y.-J. Heo, Y.-S. Jung, K. Hwang, J.-E. Kim, J.-S. Yeo, S. Lee, Y.-J. Jeon, D. Lee, D.-Y. Kim, *ACS Appl. Mater. Interfaces* **2017**, *9*, 39519.
[26] J. Zhang, Y. Zhao, J. Fang, L. Yuan, B. Xia, G. Wang, Z. Wang, Y. Zhang, W. Ma, W. Yan, W. Su, Z. Wei, *Small* **2017**, *13*, 1700388.
[27] K. Zhang, Z. Chen, A. Armin, S. Dong, R. Xia, H.-L. Yip, S. Shoaee, F. Huang, Y. Cao, *Sol. RRL* **2018**, *2*, 1700169.
[28] S. Dong, K. Zhang, B. Xie, J. Xiao, H. L. Yip, H. Yan, F. Huang, Y. Cao, *Adv. Energy Mater.* **2019**, *9*, 1802832.
[29] S. Strohm, F. Machui, S. Langner, P. Kubis, N. Gasparini, M. Salvador, I. McCulloch, H. J. Egelhaaf, C. J. Brabec, *Energy Environ. Sci.* **2018**, *11*, 2225.
[30] N. Espinosa, R. Garcia-Valverde, A. Urbina, F. C. Krebs, *Sol. Energy Mater. Sol. Cells* **2011**, *95*, 1293.
[31] R. R. Søndergaard, M. Hösel, F. C. Krebs, *J. Polym. Sci., Part B: Polym. Phys.* **2013**, *51*, 16.
[32] R. Søndergaard, M. Hösel, D. Angmo, T. T. Larsen-Olsen, F. C. Krebs, *Mater. Today* **2012**, *15*, 36.
[33] F. C. Krebs, R. Søndergaard, M. Jørgensen, *Sol. Energy Mater. Sol. Cells* **2011**, *95*, 1348.
[34] S. Li, L. Zhan, F. Liu, J. Ren, M. Shi, C. Z. Li, T. P. Russell, H. Chen, *Adv. Mater.* **2018**, *30*, 1705208.
[35] S. Oh, S. Badgujar, D. H. Kim, W. E. Lee, N. Khan, M. Jahandar, S. Rasool, C. E. Song, H. K. Lee, W. S. Shin, J. C. Lee, S. J. Moon, S. K. Lee, *J. Mater. Chem. A* **2017**, *5*, 15923.
[36] X. Dong, P. Shi, L. Sun, J. Li, F. Qin, S. Xiong, T. Liu, X. Jiang, Y. Zhou, *J. Mater. Chem. A* **2019**, *7*, 1989.
[37] S. Wang, Y. Zhao, H. Lian, C. Peng, X. Yang, Y. Gao, Y. Peng, X. Lan, O. I. Elmi, D. Stievenard, B. Wei, F. Zhu, T. Xu, *Nanophotonics* **2019**, *8*, 297.
[38] T. Yan, W. Song, J. Huang, R. Peng, L. Huang, Z. Ge, *Adv. Mater.* **2019**, 1902210.
[39] L. Mao, J. Tong, S. Xiong, F. Jiang, F. Qin, W. Meng, B. Luo, Y. Liu, Z. Li, Y. Jiang, C. Fuentes-Hernandez, B. Kippelen, Y. Zhou, *J. Mater. Chem. A* **2017**, *5*, 3186.
[40] F. C. Krebs, S. A. Gevorgyan, J. Alstrup, *J. Mater. Chem.* **2009**, *19*, 5442.
[41] C. Yan, S. Barlow, Z. Wang, H. Yan, A. K. Y. Jen, S. R. Marder, X. Zhan, *Nat. Rev. Mater.* **2018**, *3*, 1.
[42] J. Yuan, Y. Zhang, L. Zhou, G. Zhang, H.-L. Yip, T.-K. Lau, X. Lu, C. Zhu, H. Peng, P. A. Johnson, M. Leclerc, Y. Cao, J. Ulanski, Y. Li, Y. Zou, *Joule* **2019**, *3*, 1.
[43] B. Fan, D. Zhang, M. Li, W. Zhong, Z. Zeng, L. Ying, F. Huang, Y. Cao, *Sci. China: Chem.* **2019**, *62*, 746.
[44] D. Qian, L. Ye, M. Zhang, Y. Liang, L. Li, Y. Huang, X. Guo, S. Zhang, Z. Tan, J. Hou, *Macromolecules* **2012**, *45*, 9611.
[45] W. Zhao, D. Qian, S. Zhang, S. Li, O. Inganäs, F. Gao, J. Hou, *Adv. Mater.* **2016**, *28*, 4734.
[46] M. B. Upama, M. Wright, M. A. Mahmud, N. K. Elumalai, A. Mahboubi Soufiani, D. Wang, C. Xu, A. Uddin, *Nanoscale* **2017**, *9*, 18788.
[47] S. I. Na, Y. H. Seo, Y. C. Nah, S. S. Kim, H. Heo, J. E. Kim, N. Rolston, R. H. Dauskardt, M. Gao, Y. Lee, D. Vak, *Adv. Funct. Mater.* **2019**, *29*, 1805825.
[48] N. Li, J. D. Perea, T. Kassar, M. Richter, T. Heumueller, G. J. Matt, Y. Hou, N. S. Güldal, H. Chen, S. Chen, S. Langner, M. Berlinghof, T. Unruh, C. J. Brabec, *Nat. Commun.* **2017**, *8*, 14541.
[49] P. Cheng, H. Bai, N. K. Zawacka, T. R. Andersen, W. Liu, E. Bundgaard, M. Jørgensen, H. Chen, F. C. Krebs, X. Zhan, *Adv. Sci.* **2015**, *2*, 1500096.
[50] Y. Firdaus, V. M. Le Corre, J. I. Khan, Z. Kan, F. Laquai, P. M. Beaujuge, T. D. Anthopoulos, *Adv. Sci.* **2019**, *6*, 1802028.
[51] S. Esiner, G. W. P. van Pruissen, M. M. Wienk, R. A. J. Janssen, *J. Mater. Chem. A* **2016**, *4*, 5107.
[52] F. J. Lim, K. Ananthanarayanan, J. Luther, G. W. Ho, *J. Mater. Chem.* **2012**, *22*, 25057.

[53] M. Välimäki, P. Apilo, R. Po, E. Jansson, A. Bernardi, M. Ylikunnari, M. Vilkman, G. Corso, J. Puustinen, J. Tuominen, J. Hast, *Nanoscale* **2015**, *7*, 9570.
[54] A. Liu, W. Zheng, X. Yin, J. Yang, Y. Lin, W. Cai, X. Yu, Q. Liang, Z. He, H. Wu, Y. Li, F. Zhang, L. Hou, *ACS Appl. Mater. Interfaces* **2019**, *11*, 10777.
[55] J. Cheng, H. Zhang, Y. Zhao, J. Mao, C. Li, S. Zhang, K. S. Wong, J. Hou, W. C. H. Choy, *Adv. Funct. Mater.* **2018**, *28*, 1706403.
[56] H. Lu, H. Lu, Y. Liu, M. Li, X. Xu, Y. Wu, Z. Bo, *Org. Electron.* **2019**, *69*, 56.
[57] L. Duan, H. Yi, Y. Zhang, F. Haque, C. Xu, A. Uddin, *Sustainable Energy Fuels* **2019**, *3*, 723.
[58] N. Y. Doumon, M. V. Dryzhov, F. V. Houard, V. M. Le Corre, A. Rahimi Chatri, P. Christodoulis, L. J. A. Koster, *ACS Appl. Mater. Interfaces* **2019**, *11*, 8310.
[59] W. C. H. Choy, D. Zhang, *Small* **2016**, *12*, 416.
[60] T. Stubhan, N. Li, N. A. Luechinger, S. C. Halim, G. J. Matt, C. J. Brabec, *Adv. Energy Mater.* **2012**, *2*, 1433.
[61] F. Guillain, D. Tsikritzis, G. Skoulatakis, S. Kennou, G. Wantz, L. Vignau, *Sol. Energy Mater. Sol. Cells* **2014**, *122*, 251.
[62] S. Höfle, M. Bruns, S. Strässle, C. Feldmann, U. Lemmer, A. Colsmann, *Adv. Mater.* **2013**, *25*, 4113.
[63] L. Ying, F. Huang, G. C. Bazan, *Nat. Commun.* **2017**, *8*, 14047.
[64] M. H. Hoang, G. E. Park, S. Choi, C. G. Park, S. H. Park, T. Van Nguyen, S. Kim, K. Kwak, M. J. Cho, D. H. Choi, *J. Mater. Chem. C* **2019**, *7*, 111.
[65] G. W. Kim, J. Lee, G. Kang, T. Kim, T. Park, *Adv. Energy Mater.* **2018**, *8*, 1701935.
[66] D. Liu, B. Yang, B. Jang, B. Xu, S. Zhang, C. He, H. Y. Woo, J. Hou, *Energy Environ. Sci.* **2017**, *10*, 546.
[67] S. J. Jeon, Y. W. Han, D. K. Moon, *ACS Appl. Mater. Interfaces* **2019**, *11*, 9239.
[68] H. Luo, C. Yu, Z. Liu, G. Zhang, H. Geng, Y. Yi, K. Broch, Y. Hu, A. Sadhanala, L. Jiang, P. Qi, Z. Cai, H. Sirringhaus, D. Zhang, *Sci. Adv.* **2016**, *2*, e1600076.
[69] J. yeong Kim, S. Park, S. Lee, H. Ahn, S. yoon Joe, B. J. Kim, H. J. Son, *Adv. Energy Mater.* **2018**, *8*, 1801601.
[70] X. Gu, Y. Zhou, K. Gu, T. Kurosawa, Y. Guo, Y. Li, H. Lin, B. C. Schroeder, H. Yan, F. Molina-Lopez, C. J. Tassone, C. Wang, S. C. B. Mannsfeld, H. Yan, D. Zhao, M. F. Toney, Z. Bao, *Adv. Energy Mater.* **2017**, *7*, 1602742.
[71] Y. Li, N. Zheng, L. Yu, S. Wen, C. Gao, M. Sun, R. Yang, *Adv. Mater.* **2019**, *31*, 1807832.
[72] H. Wu, H. Fan, S. Xu, L. Ye, Y. Guo, Y. Yi, H. Ade, X. Zhu, *Small* **2019**, *15*, 1804271.
[73] X. Xue, K. Weng, F. Qi, Y. Zhang, Z. Wang, J. Ali, D. Wei, Y. Sun, F. Liu, M. Wan, J. Liu, L. Huo, *Adv. Energy Mater.* **2019**, *9*, 1802686.
[74] L. Zhang, X. Xu, B. Lin, H. Zhao, T. Li, J. Xin, Z. Bi, G. Qiu, S. Guo, K. Zhou, X. Zhan, W. Ma, *Adv. Mater.* **2018**, *30*, 1805041.
[75] S. Pang, R. Zhang, C. Duan, S. Zhang, X. Gu, X. Liu, F. Huang, Y. Cao, *Adv. Energy Mater.* **2019**, *9*, 1901740.
[76] H. Huang, Q. Guo, S. Feng, C. Zhang, Z. Bi, W. Xue, J. Yang, J. Song, C. Li, X. Xu, Z. Tang, W. Ma, Z. Bo, *Nat. Commun.* **2019**, *10*, 3038.
[77] H. Bin, Y. Yang, Z. G. Zhang, L. Ye, M. Ghasemi, S. Chen, Y. Zhang, C. Zhang, C. Sun, L. Xue, C. Yang, H. Ade, Y. Li, *J. Am. Chem. Soc.* **2017**, *139*, 5085.
[78] C. Wang, S. Ni, S. Braun, M. Fahlman, X. Liu, *J. Mater. Chem. C* **2019**, *7*, 879.
[79] A. J. Moulé, M.-C. Jung, C. W. Rochester, W. Tress, D. LaGrange, I. E. Jacobs, J. Li, S. A. Mauger, M. D. Rail, O. Lin, D. J. Bilsky, Y. Qi, P. Stroeve, L. A. Berben, M. Riede, *J. Mater. Chem. C* **2015**, *3*, 2664.
[80] B. H. Lee, I. H. Jung, H. Y. Woo, H. K. Shim, G. Kim, K. Lee, *Adv. Funct. Mater.* **2014**, *24*, 1100.
[81] J. Cheng, F. Xie, Y. Liu, W. E. I. Sha, X. Li, Y. Yang, W. C. H. Choy, *J. Mater. Chem. A* **2015**, *3*, 23955.
[82] Y. W. Han, H. J. Song, S. J. Jeon, H. S. Lee, E. J. Ko, C. E. Song, T. H. Sung, D. K. Moon, *J. Mater. Chem. A* **2019**, *7*, 14790.
[83] Y. Guo, H. Lei, L. Xiong, B. Li, Z. Chen, J. Wen, G. Yang, G. Li, G. Fang, *J. Mater. Chem. A* **2017**, *5*, 11055.
[84] A. Y. Al-Ahmad, J. Holdsworth, B. Vaughan, G. Sharafutdinova, X. Zhou, W. J. Belcher, P. C. Dastoor, *Prog. Photovoltaics* **2019**, *27*, 179.
[85] C. L. Cutting, M. Bag, D. Venkataraman, *J. Mater. Chem. C* **2016**, *4*, 10367.
[86] Y. Wang, B. Wu, Z. Wu, Z. Lan, Y. Li, M. Zhang, F. Zhu, *J. Phys. Chem. Lett.* **2017**, *8*, 5264.
[87] S. R. Cowan, A. Roy, A. J. Heeger, *Phys. Rev. B* **2010**, *82*, 245207.
[88] B. Qi, J. Wang, *Phys. Chem. Chem. Phys.* **2013**, *15*, 8972.
[89] Y. X. Zhang, C. Gao, J. De Chen, W. Li, Y. Q. Li, J. X. Tang, *J. Mater. Chem. A* **2018**, *6*, 11830.
[90] T. Nagata, S. Oh, T. Chikyow, Y. Wakayama, *Org. Electron.* **2011**, *12*, 279.
[91] H. Park, S. H. Lee, F. S. Kim, H. H. Choi, I. W. Cheong, J. H. Kim, *J. Mater. Chem. A* **2014**, *2*, 6532.
[92] L. Ouyang, C. Musumeci, M. J. Jafari, T. Ederth, O. Inganas, *ACS Appl. Mater. Interfaces* **2015**, *7*, 19764.
[93] Y. W. Han, J. Y. Choi, Y. J. Lee, E. J. Ko, M. H. Choi, I. S. Suh, D. K. Moon, *Adv. Mater. Interfaces* **2018**, *6*, 1801396.
[94] L.-M. Chen, Z. Hong, G. Li, Y. Yang, *Adv. Mater.* **2009**, *21*, 1434.
[95] Y. Liu, Y. Zhao, S. Xu, S. Cao, *Polymer* **2015**, *77*, 42.
[96] C. M. Palumbiny, F. Liu, T. P. Russell, A. Hexemer, C. Wang, P. Muller-Buschbaum, *Adv. Mater.* **2015**, *27*, 3391.
[97] L. Lucera, P. Kubis, F. W. Fecher, C. Bronnbauer, M. Turbiez, K. Forberich, T. Ameri, H. J. Egelhaaf, C. J. Brabec, *Energy Technol.* **2015**, *3*, 373.
[98] N. Espinosa, M. Hösel, D. Angmo, F. C. Krebs, *Energy Environ. Sci.* **2012**, *5*, 5117.